3-Dimensional Adaptive Unstructured Tessellated Look-up Tables for the Approximation of Compton Form Factors

Charles Hyde [©] ^a, Mitch Kerver^a, Christos Tsolakis [©] ^b, Polykarpos Thomadakis^b, Spiros Tsalikis [©] ^b, Kevin Garner [©] Angelos Angelopoulos^b, Wirawan Purwanto^c, Gagik Gavalian^d, Christian Weiss^d, Nikos Chrisochoides ^{a,b,*}

^aDepartment of Physics, Old Dominion University, Norfolk, VA, USA
 ^bCRTC, Department of Computer Science, Old Dominion University, Norfolk, VA, USA
 ^cDivision of Digital Transformation and Technology, Old Dominion University, Norfolk, VA, USA
 ^dThomas Jefferson National Accelerator Facility, Newport News, VA, USA

Abstract

We describe an iterative algorithm to construct an unstructured tessellation of simplices (irregular tetrahedra in 3-dimensions) to approximate an arbitrary function to a desired precision by interpolation. The method is applied to the generation of Compton Form Factors for simulation and analysis of nuclear femtography, as enabled by high energy exclusive processes such as electron-proton scattering producing just an electron, proton, and gamma-ray in the final state. While producing tessellations with only a 1% mean interpolation error, our results show that the use of such tessellations can significantly decrease the computation time for Monte Carlo event generation by ~ 23 times for 10^7 events (and using extrapolation, by ~ 955 times for 10^{10} events).

Keywords: Tessellation, Compton Scattering, Nuclear Femtography, Deep Exclusive, DVCS

1. Introduction

1.1. Nuclear Femtography

Quantum Chromodynamics (QCD) is a comprehensive theory of the binding of atomic nuclei, and the structure of subatomic particles including protons and neutrons. In the past two decades, new theoretical concepts and experimental techniques have emerged that for the first time enable the construction of spatial images of quarks and gluons inside the proton and other atomic nuclei [1]. The experimental processes are given the generic name Deep Virtual Exclusive Scattering (DVES). In the case of electron proton scattering ($ep \rightarrow eX$), DVES events have the general topology of

$$e + p \to e' + p' + m,\tag{1}$$

where e', p' refer to the electron and proton in the final state, and m refers to either a meson $(e.g., \pi^0, \rho, \phi...)$ or high energy gamma-ray (γ) in the final state.

Past and continuing efforts of DVES experiments include HERA [2, 3], HERMES [4], COMPASS[5], and Jefferson Lab [6, 7, 8, 9, 10] with a major program expected at the U.S. Electron Ion Collider (EIC) [11] starting in the early 2030s. For a given luminosity \mathcal{L} (measured in cm⁻²sec⁻¹) of ep collisions, the event rate for a particular process such as Eq. 1, is given by the product of luminosity times cross section:

$$Rate = \mathcal{L}\sigma \tag{2}$$

^{*}Corresponding author. E-mail address: nikos@cs.odu.edu

Since there are a minimum of three particles to detect in the final state of a DVES process, the cross section is differential in at least five independent variables—nine momentum variables reduced by four constraints from energy and momentum conservation. The functional behavior of the cross section on these five variables is determined by a convolution of factors determined from the fundamental QCD theory, together with a series of functions, called Generalized Parton Distributions (GPDs). GPDs encode the as yet unknown spatial distributions of quarks and gluons in the target proton (or other target nucleus). The connection between the GPDs and the cross section on the one hand, and GPDs and spatial imaging on the other hand, will be described in more detail in the following.

The complexity of the reactions of Eq. 1 and the even greater complexity of the detectors required to observe them necessitates extensive simulations of both the functional behavior of the differential cross sections and the response of the detector. This process is computationally intensive and must also be flexible. It is not yet possible to calculate the GPDs directly from the fundamental QCD theory, so we must rely on models, based on partial understanding of the theory together with existing data. Since these models evolve with advances in the field, the computational framework must be adaptable.

In this paper, we describe algorithms to adaptively and efficiently create tessellated look-up tables of a set of functions called Compton Form Factors (CFFs). The CFFs are functions of three kinematic variables (variables determined event-by-event in a DVES experiment). The CFFs are computed from GPDs via numerically challenging improper integrals. The CFFs are the natural interface between theory and experiment, as they are universal process-independent functions (*i.e.*, do not depend upon the final state meson in Eq. 1) and the cross section for any process can be directly calculated from the CFFs without additional numerical integration. The purpose of the tessellation procedure is as follows:

- Obtain a look-up table such that interpolation on the table will globally reproduce the input model to any predetermined precision (e.g., 1%).
- Obtain the look-up table of minimal size in a minimal number of computations of discrete CFF values. This minimizes the computation time and storage requirements for each update or new GPD model.

1.2. Tessellations and Monte Carlo Event Generation

In order to either predict the sensitivity of a proposed DVES measurement, or to analyze the data from such an experiment, it is essential to simulate the response of the experimental detector to a large statistical ensemble of simulated pseudo-events. For a given final state channel of Eq. 1, millions of random (Monte Carlo) pseudo-events are generated to comprehensively sample the experimental phase-space. Two basic approaches are followed in these studies,

- Events are generated uniformly in the multi-dimension phase space (e.g., 5-D for DVES) and each event is given a numerical weight proportional to the differential cross section.
- Events are generated by an appropriate algorithm such that the distribution of pseudo events is proportional to the differential cross section.

2. Background

2.1. Physics

Deeply Virtual Exclusive Scattering provides a means to create 3-d tomographic images of nucleons and atomic nuclei. Parton Distribution Functions (PDFs) from Deep Inelastic Scattering experiments have been able to provide information about the longitudinal momentum distribution of partons, pointlike constituents later confirmed to be the quarks and gluons which make up nucleons[12, 13]. These functions can be generalized to provide transverse spatial distributions of partons as a function of their longitudinal momentum fraction in nucleons (neutrons or protons). These functions are known as Generalized Parton Distributions (GPDs). GPDs can be accessed through Deeply Virtual Compton Scattering(DVCS), where an electron is scattered off a quark within a nucleon and emits a real photon in the final state. In the $e + N \rightarrow e + N + \gamma$ exclusive photo-production reaction, the cross section is the coherent sum of the Bethe-Heitler and Compton amplitudes, making it impossible to distinguish between the two processes

experimentally. However, contributions from the Bethe-Heitler process can be computed from QED as a function of the nucleon Form Factors leaving the DVCS amplitude given by:

$$|T_{DVCS}|^2 = \frac{e^6}{y^2 Q^2} \{ \Sigma c_n cos(n\phi_{\gamma\gamma}) + \Sigma s_n sin(n\phi_{\gamma\gamma}) \}$$
 (3)

Where c_n and s_n are coefficients involving the CFFs [14]. ξ and t can be accessed experimentally from the process kinematics. However, x is not accessible, but rather integrated over in experiments. Therefore, the quantities that can be extracted from experiments are not the GPDs themselves, but the principal value integral of the GPDs, known as Compton Form Factors (CFFs).

$$\mathcal{H}_{q}(\xi, t; Q^{2}) = \int_{-1}^{1} H_{q}(x, \xi, t; Q^{2}) \left[\frac{1}{x - \xi + i\epsilon} \pm \frac{1}{x + \xi - i\epsilon} \right] dx$$

$$= \mathcal{P} \int_{-1}^{1} \left[\frac{H_{q}(x, \xi, t; Q^{2})}{x - \xi} \pm \frac{H_{q}(x, \xi, t; Q^{2})}{x + \xi} \right] dx + i\pi \left[-H_{q}(\xi, \xi, t) \pm H_{q}(-\xi, \xi, t) \right]$$
(4)

2.2. Monte Carlo Event Generators

Monte Carlo event generators are of central importance in nuclear physics for bridging theory to experiment. As such, many popular Monte Carlo event generators have been made for high energy *ep*, *pp*, and *AA* collisions. Specific generators for *ep* collisions include Pythia [15, 16], Herwig, and FOAM. When using a general purpose Monte Carlo event generator, some specific, user implemented, physics model for each event is required. With more complex and computationally intensive models, it can be beneficial to divide the domain into smaller cells. This concept is the basis of both this paper and the FOAM event generator. Although similar in purpose, this project differs greatly in its implementation and benefits from FOAM. FOAM divides the integration domain into hyperrectangles with an algorithm that uses binary splitting, while this paper uses simplices. The benefits of simplices is further explained in section 2.3.1. FOAM's purpose is to act as a general purpose event generator, while this project focuses on generating tessellations of data to be used by other event generators. Using FOAM requires making calls to the physics model during the event generation. However, once a tessellation of a function is made, it can easily be stored and shared as a lookup table for use in other event generators without calling the physics model.

2.3. Tessellations

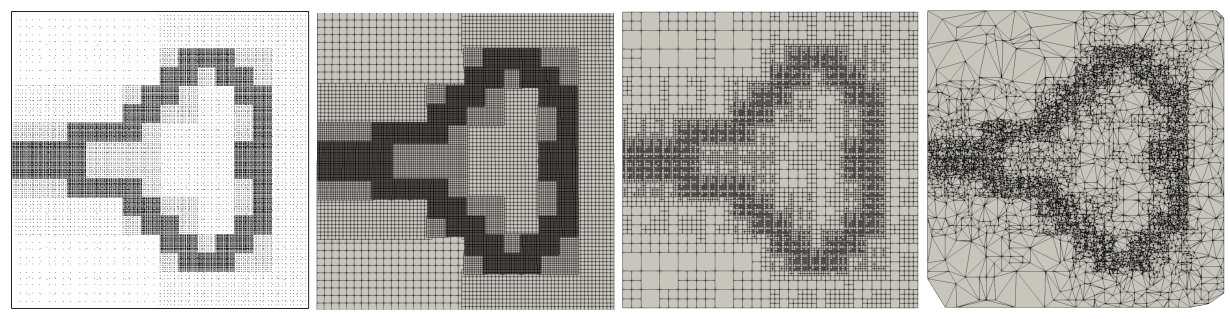
Tessellations constitute an integral part of many computational methods. They provide a discretization of the problem space which enables the application of simpler methods to each discrete element instead of dealing with the whole complexity of the domain at once. Applications of tessellations span from engineering problems where the goal is the simulation of air flow around vehicles [17] to bio-mechanical applications [18] where the focus is the deformation of brain tissues during surgery.

In this work, tessellations are utilized as an enabling technology that allows for the creation of look-up tables, enhancing the Monte-Carlo simulations used in Compton Form Factor calculations (see section 4).

2.3.1. Types of Tessellations

The plethora of applications that utilize tessellations have different requirements and restrictions. Naturally, this has created a wide variety of tessellation methods [19]. Early approaches used structured tessellations that arise naturally from the matrix formulation of many problems [19]. The problems of interest rarely have uniform characteristics throughout the computational space. The ability to concentrate more points at regions of interest to reduce the discretization error becomes a necessity. Elliptic and hyperbolic methods [20] provide a solution to this problem by tweaking the point density at regions of interest. Still, they are bound to the initial point distribution and they are limited by the complexity of the domain. Multi-block methods (see Figure 1b) [21] provide another way to capture features of the problem by overlaying uniform tessellations of different density. Octree methods [22] utilize quad-tree (2D) and oct-tree (3D) structures (see Figure 1c) that can capture the features of the problem by using a low count

of elements while at the same time providing a data structure that favor queries. Yet another method is the use of unstructured simplices (see Figure 1d) that not only further reduce the number of points and elements but are able to scale into higher dimensions at low cost.



(a) Input Dataset. A uniform tessellation (b) Multiblock tessellation capturing (c) Quad-tree tessellation capturing fea- (d) Unstructured simplices (triangles) would require 62,000 points in order to features of the input (59,000 points) capture the smallest features

capturing features of the input (7,500

Figure 1: Different types of tessellations applied on a dataset.

	2-cube	3-cube	4-cube	5-cube	2-simplex	3-simplex	4-simplex	5-simplex
0-face (vertex)	4	8	16	32	3	4	5	6
1-face (edge)	4	12	32	80	3	6	10	15
2-face	1	6	24	80	1	4	10	20
3-face		1	8	40		1	5	15
4-face			1	10			1	16
5-face				1				1

Table 1: Number of lower dimensional faces of n-dimensional cube and simplex elements

Table 1 summarizes the number of lower dimensional elements contained by each element at different dimensions. Notice that the number of vertices scales linearly for simplices while for box-based elements, the growth rate is exponential. This characteristic is crucial for the approach of this work since it enables the generalization of the method from Compton Form Factor calculations (see section 2.1) to Deeply Virtual Compton Scattering calculations which utilize 5 dimensions and Deep Virtual phi-meson Production calculations which can utilize up to 7 dimensions.

3. Mesh Generation

3.1. Input

To generate a tessellation of a function, raw data from a model must first be converted to an image-based file format that an image-to-mesh conversion software can understand/process. The file format that we chose is NRRD [23], because it can support up to 16 dimensions. Once the dimensionality, spacing, and limits of phase space are defined, the model is called and the ITK library [24] is used to store the value of the function in an NRRD file as points on a regular Cartesian lattice. Figure 2 shows a visualization (generated using Paraview [25]) of images of the $Im(H_u)$ and $Re(H_u)$ Compton Form Factor generated from *PARTONS*. The data was generated on a 41x13x81 grid in the kinematic variables $[\sqrt{t'/0.5GeV^2}, \log_2(Q^2), \log(X_{\xi})]$ so that several orders of magnitude could be covered in Q^2 and X_{ξ} , while maintaining a near cube hyperrectangle for the ease of visualization. The value of the CFF is stored only at the vertices of the grid, but Paraview's linear interpolation scheme is being used to approximate the function continuously over the entire domain as indicated by the coloring in the visualization.

3.2. Image-to-mesh conversion software

The image-to-mesh conversion software utilized is called PODM [26]. PODM is a state-of-the-art image-to-mesh conversion software capable of generating in parallel meshes of guaranteed quality, while maintaining fidelity with respect to the boundary of the input image. PODM converts images to tetrahedral meshes using proven sampling techniques. The sampling of the mesh (volume and surface) is controlled by the parameter delta (δ), where $\delta > 0$. A

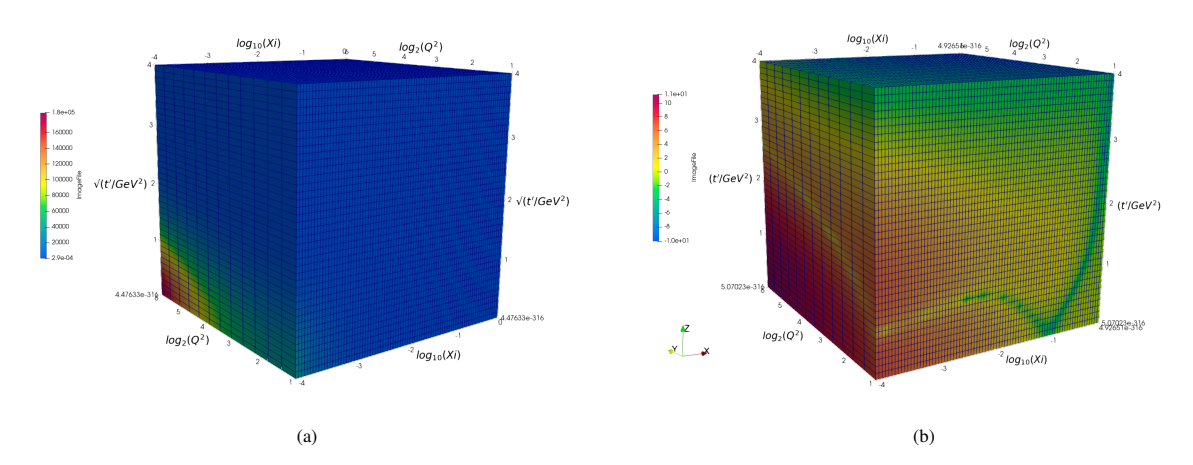


Figure 2: Cartesian Image of (a) the $Im(H_u)$ CFF and (b) $Re(H_u)$. Vertical axis is $\sqrt{t'/0.05 \text{GeV}^2}$. The horizontal axes are $\log_2(Q^2/\text{GeV}^2)$ (y) and $\log_{10} \xi$ (x).

low value of δ indicates that the sampling is denser. Ideal values of δ are considered to be multiples of the spacing of the image. To guarantee quality and fidelity, PODM employs a set of rules that split specific elements when needed. In conjunction with these rules, a user-defined rule can be specified as a sizing function, which is also used to split elements. The user-defined rule can be utilized to adapt the mesh to the input data, and it can be loaded as a shared library that PODM will utilize on-demand.

3.2.1. Portability

A Docker image containing *PODM* and *PartonsToNRRD* has been created for easy distribution to users. The software operates directly from within a Docker container and all processing happens within it. Data is transferred from a user machine to the Docker container via the use of bind mounts or volumes. Input is read from a user's computer, processed inside the Docker container, and then the output is written back to the user's computer. There are many benefits to this approach, including portability, ease-of-use, and isolation (*i.e.*, the isolation offered by Docker technologies, meaning no files are created on the base system). In addition, the usage of Docker ensures the creation of a well-defined runtime environment in which the software has been tested and verified by software developers. Users can simply load the Docker image, spawn a Docker container, and start using the software immediately. The Docker image contains a lightweight distribution of Debian Linux, *PODM*, utilities, and all the libraries required for the software to run. The Docker image can be used on all operating systems that Docker supports, including Windows, Linux, and macOS. More information regarding their repositories and how one can use these methods is described in the appendix.

3.3. Interpolation Error

Tessellations, as discussed in section 2, provide an efficient way to store data with a few number of vertices. During Monte Carlo event generation, this data needs to be quickly accessed at any given point in the domain, which requires an interpolation method to be used between vertices of the tessellation. The linear interpolation method used is described in detail in section 3.5.2. Approximating the value of a non-linear function with linear interpolation introduces an error. The method which generates the tessellations and later refines them should aim to minimize the global interpolation error. Therefore, before the different approaches to mesh generation are explored, the method of evaluating interpolation error must be defined.

To evaluate the significance of the interpolation error, sample points are generated at the barycenter of each simplex in the tessellation. At each sample point, the function is evaluated by the GPD model and compared to the linear interpolation value using the relative error, *i.e.*, relative error = $\frac{PARTONS \text{ value-linear interpolation value}}{max(PARTONS \text{ value,linear interpolation value})}$. With functions that have both positive and negative values varying over several orders of magnitude, the relative error can surge up

to infinity for values close to zero. For these values, it is more useful to look at their absolute error, *i.e.*, *absolute* error = PARTONS value - linear interpolation value. The interpolation error of each simplex is then defined as min(absolute error, relative error). This guarantees that most values will use the relative error while the absolute error is only used as the function approaches zero.

3.4. Mesh generation approaches

In addition to minimizing the number of calls to the GPD model, and thus minimizing the number of tessellation vertices, the tessellation should also be generated in a way that minimizes the global interpolation error. Generating a tessellation with a pre-specified interpolation precision and with a minimal computation cost is a difficult task. For this reason, we tried four different approaches of mesh generation. The first method generates uniform images (grids) while the remaining three methods start with the same initial image of 43,173 points as described in section 3.1.

3.4.1. Structured Tessellation

In the first approach, structured tessellations (images) are generated with varying numbers of points across each dimension. The more the points across each dimension, the smaller the size of the cubic elements become, thus lowering the interpolation error. Once an initial tessellation is generated, it is checked to see if it meets the desired error threshold. If it does not, the number of points in one or many dimensions is increased. In the case of the $Im(H_u)$ CFF, as seen in Figure 3, we increased the number of points only in the $log_{10}(\xi)$ dimension, because the behavior of the function in ξ is more complex. This loop should continue until the desired precision is met. This approach has several disadvantages: (1) the number of points required across each dimension to meet the desired precision is unknown, (2) a dense *uniform* tessellation has many elements, (3) generating a dense tessellation requires numerous GPD calculations (of which a majority would be wasted on elements that already have a sufficient interpolation error), and (4) for each instance, the GPD model must be called for *all* the points.

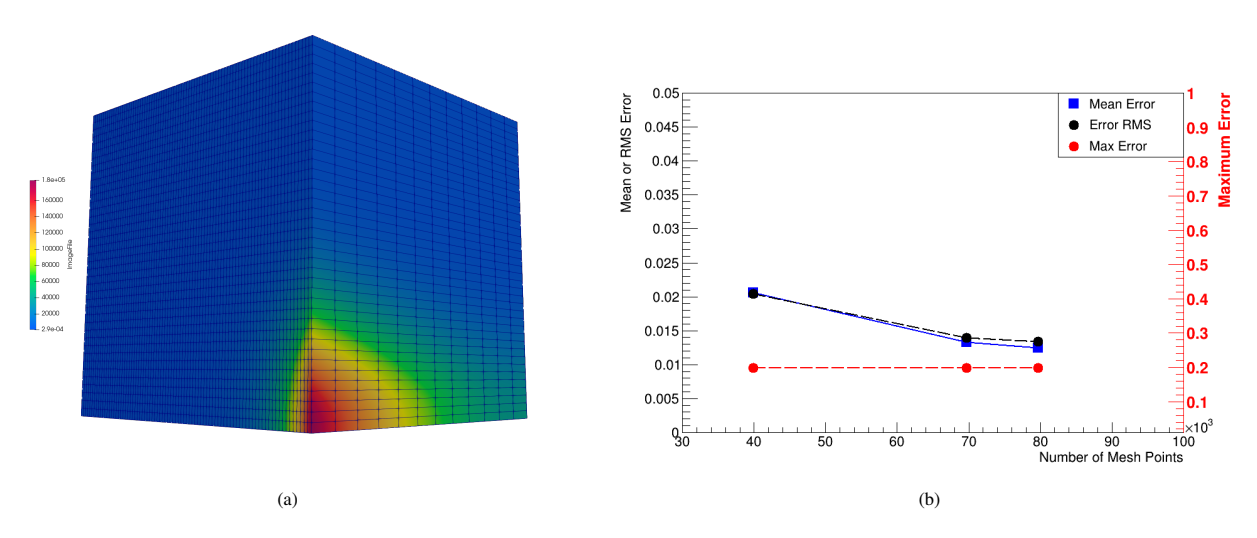


Figure 3: (a) Structured grid of $Im(H_u)$ CFF and (b) Mean, RMS, and Max interpolation error statistics of structured grids of different sizes

3.4.2. Unstructured Uniform Tessellation

In the second approach, unstructured uniform tessellations are generated with varying values of δ to control the density. The denser a uniform tessellation is, the smaller the size of the simplices become, thus lowering the interpolation error. The procedure of generating an unstructured uniform tessellation is similar to the structured approach, and although only δ needs to be updated for every instance, both have similar disadvantages. This can be seen in Figure 4 which shows the change in the mean and maximum interpolation error as the number of vertices increases. By going from approximately 77,000 vertices to about 90,000 vertices, the mean error decreases slightly. However, the maximum interpolation error remains unchanged at 40%. This confirms the need for an adaptive tessellation approach, as

many points are unnecessarily added in this uniform approach which are wasted in simplices that already have small interpolation error.

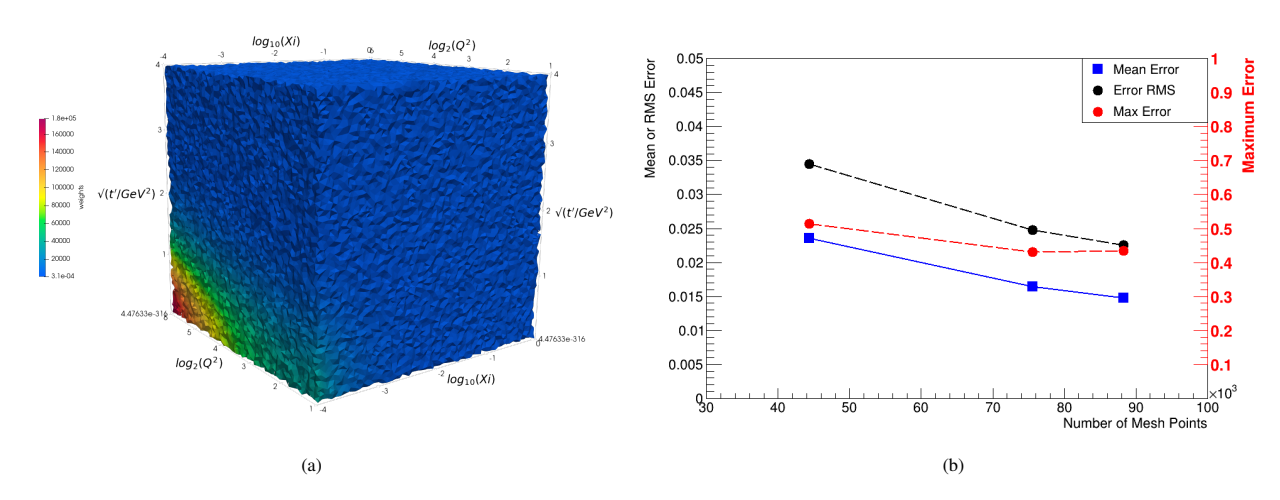


Figure 4: Uniform tessellation of $Im(H_u)$ CFF (a) the 1st instance and (b) Mean, RMS, and Max interpolation error statistics of uniform tessellations of different sizes

3.4.3. Unstructured Adaptive Tessellation

To efficiently capture the distribution of data, the tessellation needs to *adapt* to the values of the function. The goal of the third approach is to use mesh adaptation to increase the point density of the mesh where it is most needed to reduce the discretization error induced by tessellation. Adaptive tessellations are generated using two different so called *sizing functions*. We use the input image as a background (BG) mesh while refining the mesh. Before refinement, the input image is analyzed, and the *image_weight_range* = $max(image_values) - min(image_values)$ is computed. The refinement algorithm queries the sizing function (SF) to verify whether each element satisfies the user constraints. Each time the SF is called upon an element, it creates a set of sampling points SP out of the element along with their set of values V queried from the BG. As Figure 5a indicates, SP consists of the element's vertices, barycenter, and midpoints of vertices and barycenter. The points that are preserved out of SP are those that lie within the SF mesh. Finally, we compute the SF element_weight_range = SF matrix SF mesh. Finally, we compute the SF mesh. Finally, we compute the SF mesh mesh mesh adaptive tessellation needs to the values of the function.

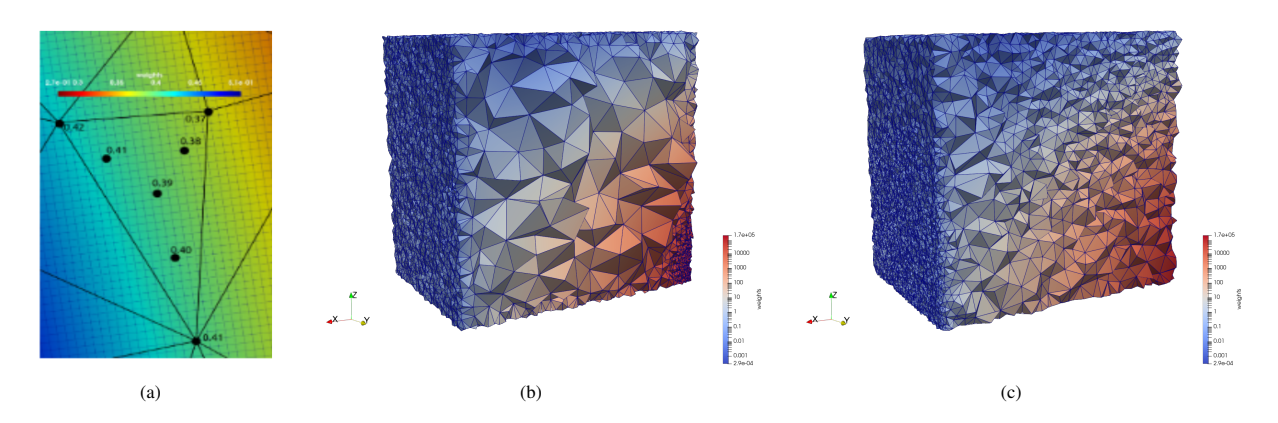


Figure 5: (a) The adaptation rule applied on a 2D element, (b) an adaptive tessellation of $Im(H_u)$ CFF using SF_1 , (c) an adaptive tessellation of $Im(H_u)$ CFF using SF_2 .

The first version (SF_1) of this sizing function splits an element if $\frac{element_weight_range}{image_weight_range}$ is greater than a user-defined $weight_limit$. As Figure 5b illustrates, SF_1 captures the behavior of the function by creating many simplices where the value of the function is large, which is not necessarily areas where the interpolation error is large.

The second version (SF_2) of this sizing function splits an element if $\frac{element_weight_range}{|average(V)|}$ is greater than a user-defined $weight_limit$. As Figure 5c illustrates, SF_2 works such that points are added more densely in regions where the function is rapidly changing, and less points are used in areas where the function is relatively constant.

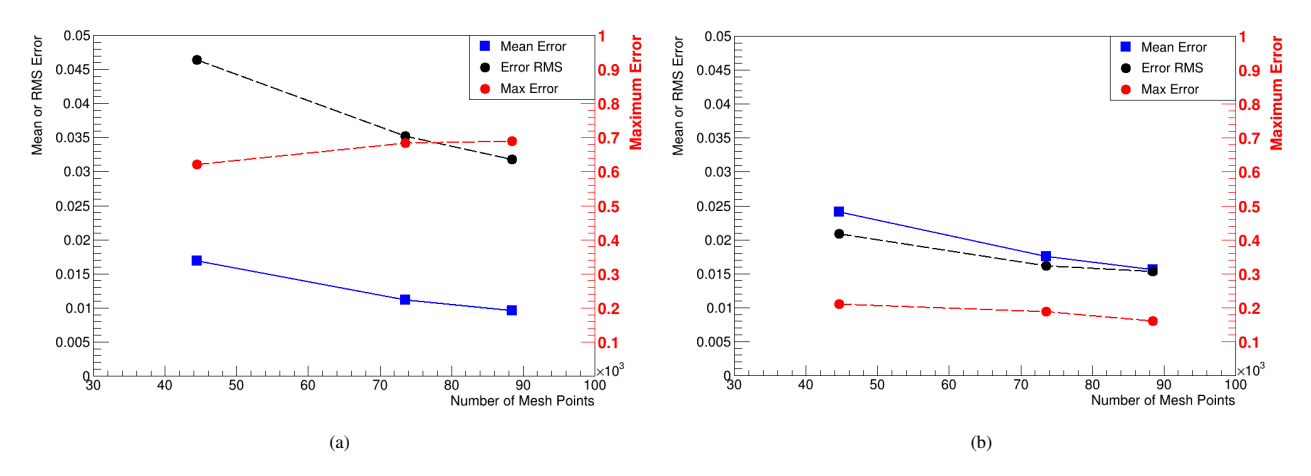


Figure 6: Mean, RMS, and Max interpolation error statistics of different mesh sizes of the $Im(H_u)$ CFF using (a) the SF_1 and (b) the SF_2 .

The plot in Figure 6a shows that the SF_1 produces a tessellation with a worse error precision compared to a uniform mesh with a similar number of vertices. Figure 6b depicts that the SF_2 produces a tessellation that has a lower average interpolation error for a given number of points compared to both the uniform and SF_1 methods. However, the maximum interpolation error continues to remain relatively constant.

3.4.4. Unstructured Iterative-Adaptive Tessellation

Computational Fluid dynamics (CFD) applications [27] [28] have shown that if the mesh is iteratively adapted based on an error estimator, the error can converge much faster than further refining the mesh in a uniform way. Leveraging this idea, Figure 7 showcases how a GPD model (*i.e.*, a "solver") can be utilized to define an error estimator for an iterative-adaptive pipeline. In this pipeline, the GPD model (in this case GPDGK16 of PARTONS) is interchangeable and the sizing function is configurable.

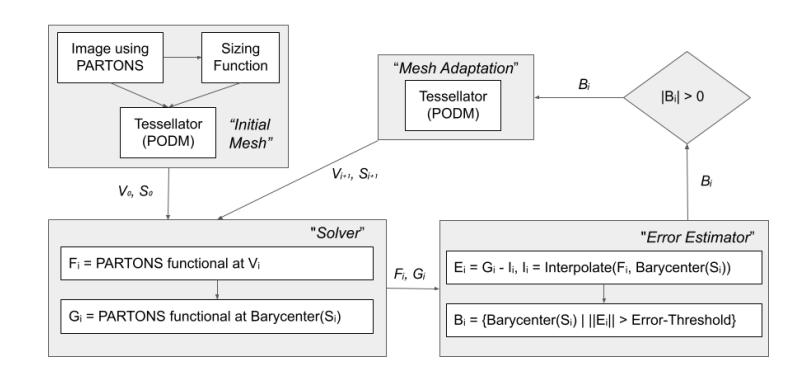
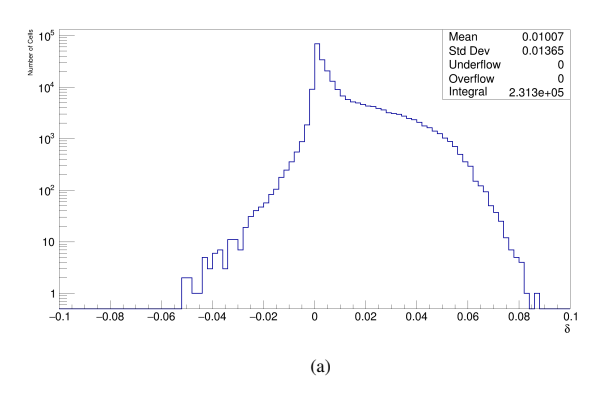


Figure 7: Iterative-adaptive pipeline for CFF data using PARTONS as the solver for error estimation.

The fourth approach of mesh generation utilizes the interpolation error as a metric for *iterative-adaptation*. As a starting point, an adaptive tessellation is generated using the SF_2 . Subsequently, for every simplex's barycenter, the value of the function is calculated from both the GPD model and from linear interpolation of the vertices of that simplex. If the interpolation error of a simplex, as defined in section 3.3, is greater than the user-defined error threshold, then the simplex's barycenter is added as a new point to the mesh of the next iteration. This iterative process continues until all simplices satisfy the specified error threshold. It should be noted that simplices which satisfy the specified error threshold are not checked again in subsequent iterations. This optimization is of utmost importance since it minimizes the number of calls to the GPD model.

Figures 8a and 8b demonstrate how after 5 iterations the distribution of interpolation errors not only narrows, but the tails of the distribution also disappear up to the value of the specified error threshold of 0.05 using the relative error metric. This shows how the iterative method specifically targets simplices with large interpolation error for refinement.



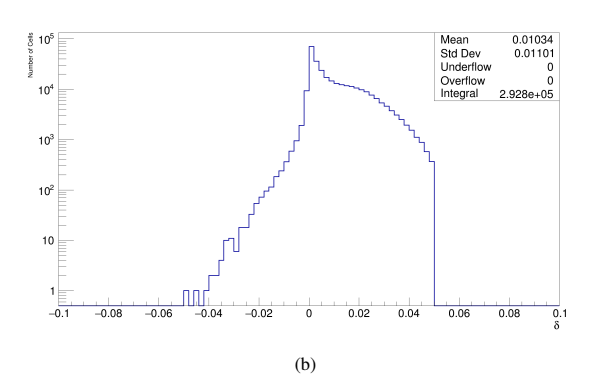
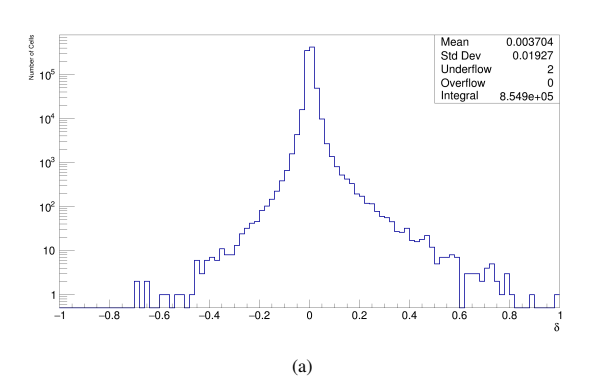


Figure 8: Histograms of the interpolation error of adaptive-iterative meshes of the $Im(H_u)$ CFF for (a) the 1st iteration and (b) the 6th iteration using the *relative error* metric.



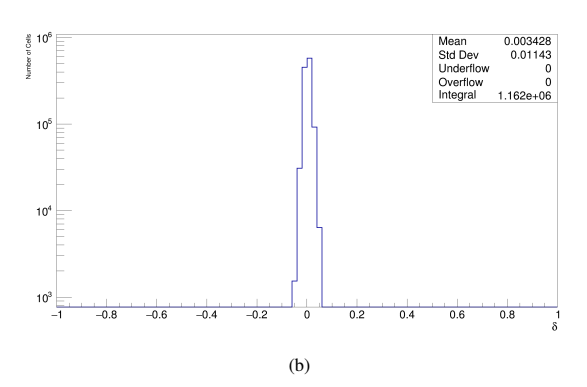


Figure 9: Histograms of the interpolation error of adaptive-iterative meshes of the $Re(H_u)$ CFF for (a) the 1st iteration and (b) the 11th iteration using the min(relative, absolute) error metric.

Figure 10a shows how this iterative-adaptive process quickly reduces both the mean interpolation error and the maximum interpolation error. However, as explained in section 3.3, the *relative error* increases significantly when the function has very small positive and negative values. To demonstrate this issue, the iterative process was applied to the $Re(H_u)$ CFF, which has both positive and negative values, and has very large relative interpolation errors as the function approaches zero. Figure 10b shows that this definition of interpolation error will result in a large maximum error, regardless of how many vertices are added (even up to 6 million vertices). This is why it is necessary to define the interpolation error as $min(absolute\ error, relative\ error)$. Using this interpolation error as a metric to guide the iterative-adaptation, both functions tested were refined until a maximum interpolation error of 0.05 was met. Figures 11a & 11b depict how this iterative-adaptation method succeeds in achieving the desired maximum interpolation

error. For the $Im(H_u)$ CFF, the desired maximum interpolation error of 5% was met in just 6 iterations and 54,500 vertices. Similarly, for the $Re(H_u)$ CFF, an average error of 0.2% and maximum error of 5% was met in 11 iterations and 192,000 vertices. The narrowing of the interpolation error distributions can be seen in Figure 9.

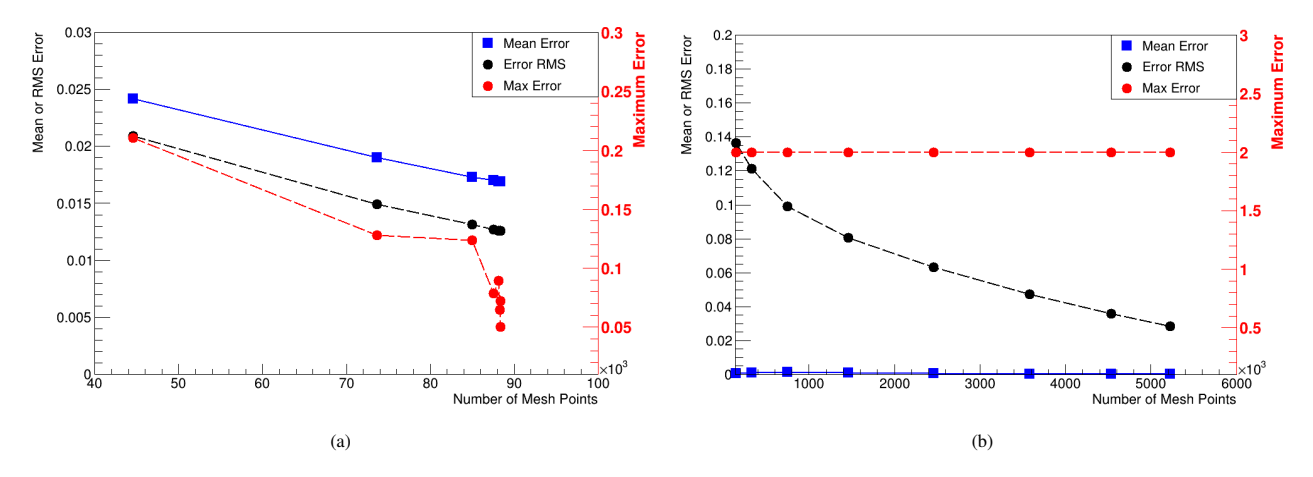


Figure 10: Mean, RMS, and Max interpolation error statistics of different mesh sizes of the (a) $Im(H_u)$ CFF and (b) $Re(H_u)$ CFF using the *relative error* metric.

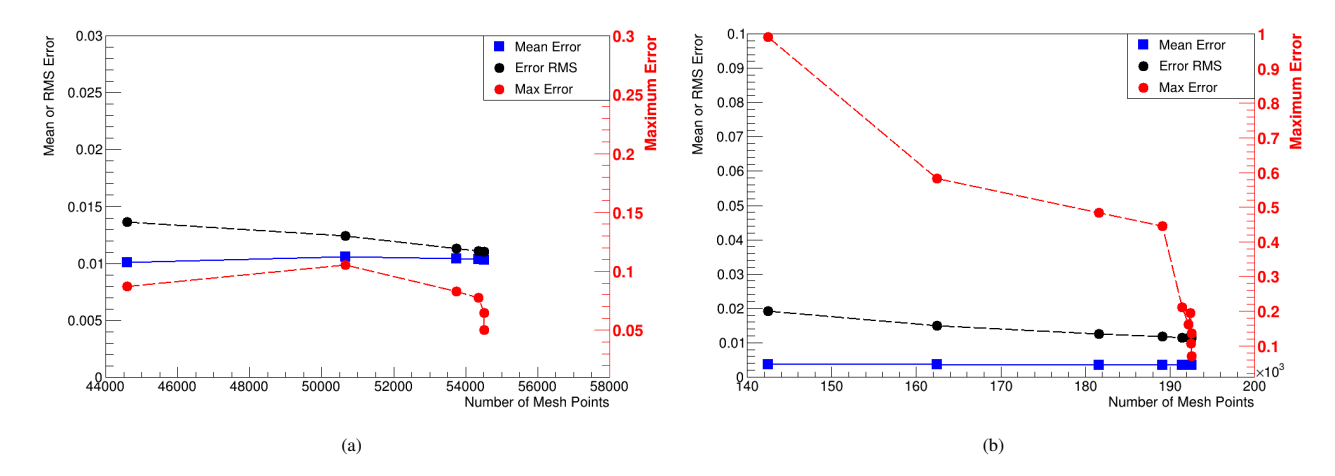


Figure 11: Mean, RMS, and Max interpolation error statistics of different mesh sizes of the (a) $Im(H_u)$ CFF and (b) $Re(H_u)$ CFF using the min(relative, absolute) error metric.

3.5. Tessellation utilities

A tessellation by itself is just a data structure. To access that data, we need certain utilities that are classified into two categories: search and numerical operations.

3.5.1. Search Operations

The most common search operation is **point location**. Given a point p, and a tessellation with N_S simplices, find the simplex S_i , where i = 0, ..., N - 1, within which p is located. This search operation is performed using the *vtkStaticCellLocator* data structure of the VTK library [29]. The *vtkStaticCellLocator* includes the functionality to perform the point location operation with worst-case time complexity $O(log(n^3))$, and it is designed to be used in parallel as well.

Another famous search operation is *find cell neighbors*. Given a simplex S_i of a tessellation, find its neighbor simplices with which it shares a face. This search operation is performed using the vtkStaticCellLinks data structure

of the VTK library [29]. This search operation has the time complexity O(1), assuming that every simplex has this information stored inside its data structure, while generating the tessellation.

3.5.2. Numerical Operations

As opposed to *Unstructured* grids, a benefit offered by *Structured* grids is that the computation of the volume of a cell, which is cubic, is trivial. On the other hand, the computation of the *volume of a simplex* is more complex. Let the points $\{X_i|i=0,...,N\}$, which are *column* vectors, define an *N*-simplex *S*. The volume of *S* is expressed with the following formula:

$$V_S = \left| det \begin{pmatrix} X_0^T & 1 \\ {X_1}^T & 1 \\ \dots & \dots \\ {X_N}^T & 1 \end{pmatrix} \right| / N!$$

The volume of a simplex is useful because it can be utilized to perform *linear interpolation in a simplex*. Let the functional values of the points be defined as $\{f_{X_i}|i=0,...,N\}$, and p be an arbitrary point inside S. Then, with an arbitrary choice of X_0 , we define a basis set for S and rhs column vector as follows:

$$\{\Delta X_i = X_i - X_0 | i = 1, ..., N\}, rhs = p - X_0$$

Afterward, we can define the interpolation weights $\{W_{X_i}|i=0,...,N\}$ as follows:

$$\forall X_i | i = 1, ..., N : W_{X_i} = det(M)/V_S$$
, where $M = N \times N$, and $M_j = \begin{cases} rhs & j = i \\ \Delta X_i & j \neq i \end{cases}$, $j = 1, ..., N$

$$W_{X_0} = N! - \sum_{i=1}^{N} W_{X_i}$$

Utilizing the interpolation weights and the functional values, we can calculate the interpolated functional value of p as follows:

$$f_p = \frac{\sum_{i=0}^{N} f_{X_i} * W_{X_i}}{\sum_{i=0}^{N} W_{X_i}}$$

4. Monte Carlo Event Generation using Look-Up Table on Tessellated Mesh

Monte Carlo event generators in nuclear femtography often want to generate the final state events according to the probability distribution defined by the differential cross section. To do so, event generators can either generate events uniformly in the phase space and weigh the events by the value of the cross section, or generate unweighted events bound by cross section distribution using an acceptance-rejection method. Both methods require in-situ calculations of the value cross section at every MC point. Additionally, the cross section can vary over several orders of magnitude leading to many rejected events in an acceptance-rejection method.

An adaptive look-up table of a tessellation of the cross section can be used to eliminate these issues and improve the efficiency of MC event generation. In the case of DVCS, the 5-fold differential cross section can be reduced to the 4-fold differential unpolarized cross section. Therefore, a 4D tessellation would be needed to be used as a look-up table of the cross section. However, the 3-dimensional Compton Form Factors that contribute to the DVCS cross section can be tessellated and used as an adaptive look-up table in the full calculation of the cross section. Since calculation of the CFFs from models is computationally expensive, querying the tessellation of a CFF as a look-up table will save

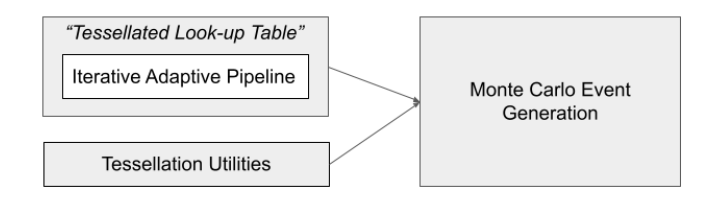


Figure 12: Monte Carlo event generation pipeline using an adaptive tessellated look-up table and the tessellation utilities.

computational efforts. The proposed Monte Carlo (MC) event generation method, which is depicted in Figure 12, can generate events using the adaptive look-up table either uniformly or using an "importance-sampling" algorithm to generate MC events according to the distribution of the CFF. First, the integral of the interpolation function of each simplex is calculated:

$$I_k = V_k \sum_{i=0}^{N} \frac{\bar{f}_j(k)}{N+1}$$
 (5)

where the volume of each simplex is extracted using the Tessellation utilities. The Riemann sum of simplex integrals is calculated and normalized to 1.

$$F_0 = 0, F_m = \frac{\sum_{k=1}^m I_k}{\sum_{k=1}^{N_s} I_k} (6)$$

Then a random MC event $u \in [0, 1]$ is generated. The simplex that is selected, using binary search, has the random event weight bounded by its Riemann sum, such that:

$$F_{k-1} \le u < F_k \tag{7}$$

The MC event, called P_{nS} , is randomly generated using a uniform distribution [30] in the selected *n*-dimensional simplex, which has X_i as vertices. The weights that are used are denoted as λ_j , j = 0, ..., n + 1.

$$P_{nS} = \sum_{i=1}^{n+1} \left((1 - \lambda_i) \prod_{j=0}^{i-1} \lambda_j \right) X_i, \text{ with } \lambda_0 = 1 \text{ and } \lambda_{n+1} = 1$$

$$\forall \lambda_j | i = 1, ..., n : \lambda_j = \sqrt[4]{z_j}, \text{ with } k = (n+1) - j$$
(8)

When performing full detector simulations for an experiment, the Monte Carlo events are often weighted by the cross section or generated according to the probability distribution defined by the cross section. However, this case study created 3-D tessellations of CFFs rather than the 5-D cross section. As a proof of concept, the tessellation utilities were used to extract the CFFs from a tessellation and generate Monte Carlo events according to the probability distribution defined by the CFF. This method of Monte Carlo event generation using an adaptive look-up table to extract the CFF from a tessellation significantly increases efficiency. Figure 13 shows a visualization of 1 million MC events generated according to the distribution of the $Im(H_u)$ Compton Form Factor. As mentioned previously, the drawback of this method is that the MC events will have a small error from the linear interpolation. The significance of the computation time saved and the performance optimizations of this method are explained in section 5.3.

5. Performance Evaluation

This performance evaluation consists of four sections. The first section shows the total run-time of the iterative-adaptive pipeline to generate a mesh of $Im(H_u)$ using (a) 40 cores, and (b) 800 cores for PARTONS, and the run-time per iteration of the iterative-adaptive pipeline steps to generate a mesh of (a) $Im(H_u)$, and (b) $Re(H_u)$ using 800 cores

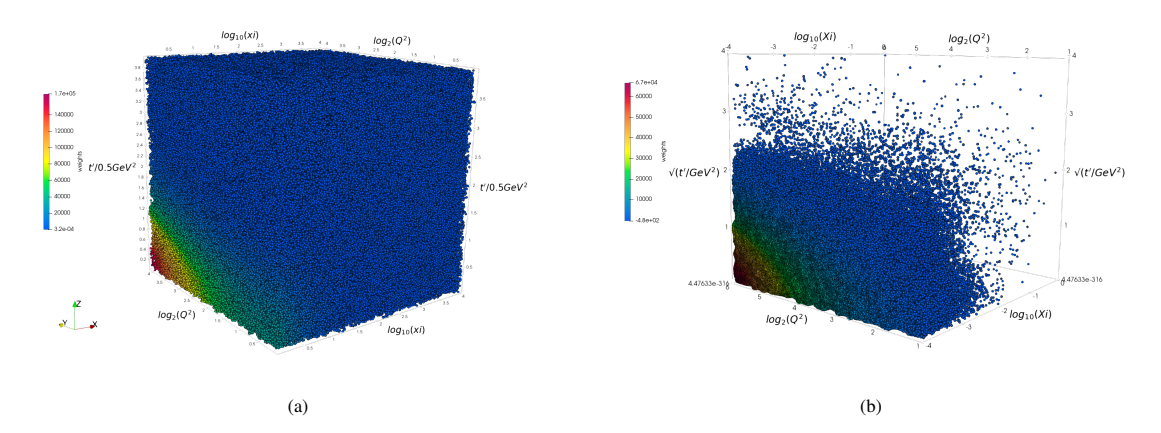


Figure 13: 1 million Monte Carlo events generated (a) uniformly and (b) according to the distribution of the $Im(H_u)$ CFF using an adaptive tessellation as a lookup table.

for PARTONS. The second section estimates the cost of generating an unstructured uniform tessellation of $Im(H_u)$ that satisfies the error threshold, and compares it with the resulting tessellation of the iterative-adaptive pipeline using 800 cores for the PARTONS. The third section showcases the benefits of generating MC events utilizing the tessellation of $Im(H_u)$ as a look-up table generated by the iterative-adaptive pipeline, compared to the GPD model using (a) 40 cores, and (b) 800 cores. All iterative-adaptive tessellations are generated using the min(relative, absolute) error metric and error threshold = 0.05.

To evaluate the performance of our results, we use the CPU nodes of Old Dominion University's Wahab HPC cluster that each have two 20-core Intel Xeon Gold 6148 2.40GHz CPUs (totaling 40 cores per node) and 384GB of RAM. The compiler that we use is GCC 7.5.0.

5.1. Run-time of Iterative-Adaptive Pipeline steps

Table 2: Iterative-Adaptive Pipeline steps.

Pipeline	Description
Step	
Meshing	The Meshing IO step includes the reading and writing of files needed for the Meshing
IO	step.
Meshing	The Meshing step includes the generation of the first mesh and the insertion of additional
	points to perform adaptive mesh refinement.
Kinematics	The Kinematics step includes the generation of input, such as initial grid points, mesh
	vertices, and barycenters, for the PARTONS step.
PARTONS	The PARTONS step includes the computation of all the CFF values of the input kine-
	matics points, such as input image grid points, mesh vertices, and the mesh simplices'
	barycenters.
PARTONS	The PARTONS IO step includes the merging of the PARTONS result of each processing
IO	core into one file.
Update	The Update Weights step includes the updating of the weights (CFF values) of the new
Weights	mesh vertices.
Compute	The Compute Error step includes the linear interpolation computation (using the tessel-
Error	lation utilities) of all the barycenters, the calculation of the linear interpolation error, and
	the writing of the points that will be added into the next iteration's mesh.

The iterative-adaptive pipeline that generates an accurate tessellation for a specific CFF consists of seven core steps as described in Table 2. It should be noted that the step of converting the PARTONS data to the initial image is omitted because it does not constitute a *full* iteration, and its cost (time-wise) is negligible. The meshing step, which utilizes the parallel software PODM, is not executed in parallel. The reasoning behind this choice is that PODM's operation of inserting additional points, which has been implemented specifically for this application, is not yet parallel. The PARTONS step has been modified to effectively utilize distributed computing nodes for parallel execution. As Figure 14 illustrates, parallelizing the PARTONS step was the most significant factor in reducing the total run-time of the pipeline. The remainder of the pipeline steps are sequential.

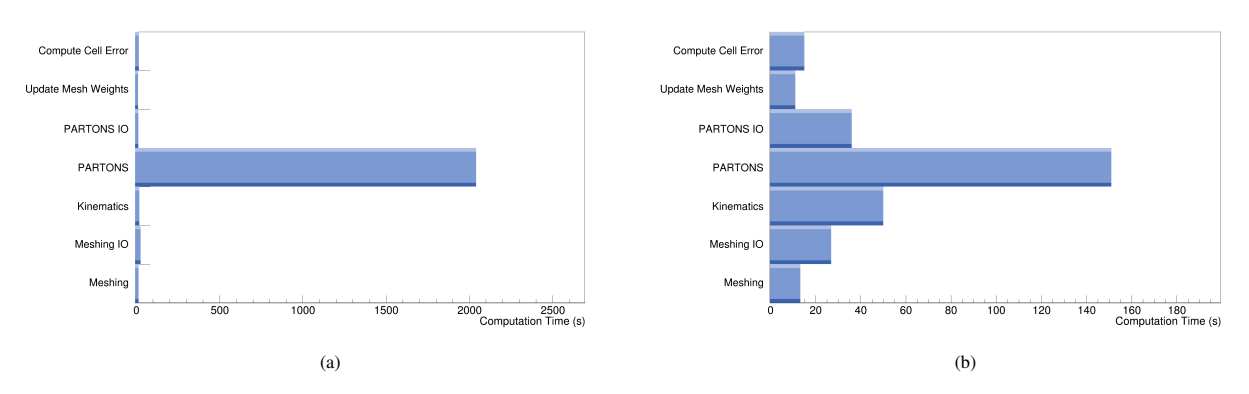


Figure 14: The total run-time of the steps in the iterative-adaptive pipeline to generate a tessellation of $Im(H_u)$ using (a) 40 cores, and (b) 800 cores for PARTONS.

In section 3.4.4, we discussed the benefit of ensuring that the iterative-adaptive pipeline knows when a simplex has already satisfied the specified error threshold in a previous iteration. Consequently, in each iteration, only the newly introduced simplices should be checked to see if they satisfy the specified error threshold. Figure 15 verifies our argument, since it showcases that while the number of points (and therefore simplices) increases per iteration, the time spent for PARTONS calls does not follow the same trend and decreases in almost every iteration.

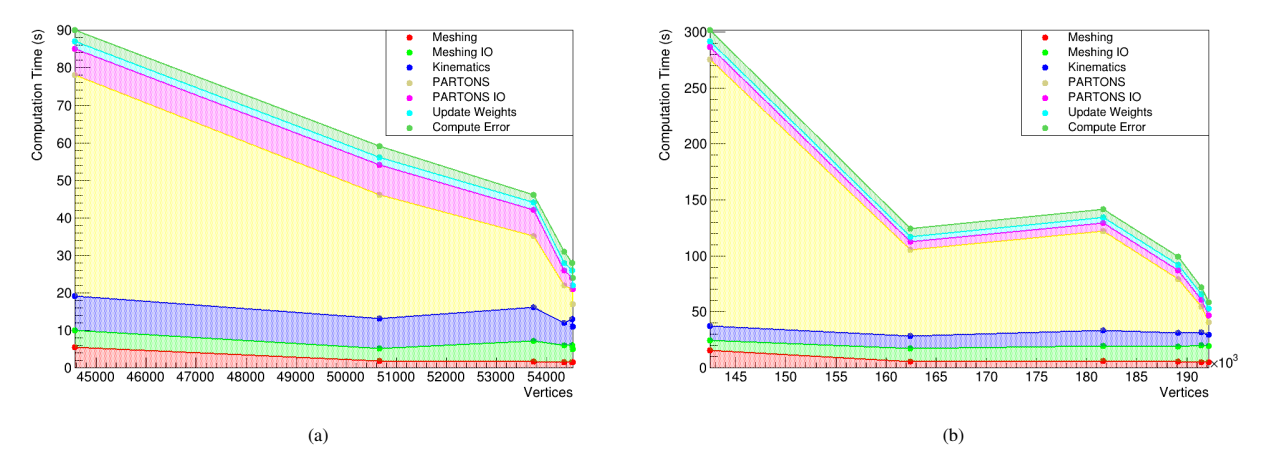


Figure 15: Shown is the run-time of each step per iteration in the iterative-adaptive pipeline to generate a mesh of (a) $Im(H_u)$, and (b) $Re(H_u)$ with a maximum interpolation error of 0.05. The widths of the individual bands correspond to the computational time of each step. The PARTONS step was executed using 800 cores.

5.2. Uniform Unstructured vs Iterative-Adaptive Unstructured

In section 3.4.2, we understood that generating a uniform unstructured tessellation, which satisfies the specified error threshold, is a task with several disadvantages. In this section, we attempt to estimate, using extrapolation techniques, the number of vertices and the computational cost that would be required to generate an accurate uniform unstructured tessellation of $Im(H_u)$ that satisfies the error threshold using 800 cores for the PARTONS. Subsequently, we compare this computational cost with that of the resulting tessellation of the iterative-adaptive pipeline using 800 cores for the PARTONS.

Table 3: Maximum interpolation error and computation cost of generating uniform unstructured tessellations of $Im(H_u)$ with different numbers of vertices.

Vertices	Max Error	Computation cost (sec)
44585	0.2066	204
73616	0.1451	319
88388	0.1129	367

Based on the data provided in Table 3, we derived the following approximation functions, using linear regression, that capture the trend of the maximum interpolation error and the computation cost: $Error_{max}(v) = -2.14*10^{-6}*v + 0.302$, and $ComputationCost(v) = 3.75*10^{-3}*v + 38.1$. Since the desired error threshold is 0.05, the estimated required number of vertices is 117,757, and the estimated required computation cost is 479 seconds. The iterative-adaptive pipeline generated a tessellation with 54,523 vertices in 309 seconds; therefore, it is better in all regards compared to the estimated uniform tessellated result.

5.3. Monte Carlo Event Generation

As described in section 4, tessellated meshes can be utilized as look-up tables for Monte Carlo (MC) event generation. Consequently, we developed a parallel software for MC simulation capable of utilizing distributed computing nodes. The purpose of this software is to demonstrate that the MC simulation can be greatly expedited using an accurate adaptive tessellation of a CFF. To validate our assumption, we (a) generate an accurate tessellation of $Im(H_u)$ using the iterative-adaptive pipeline, (b) generate 10^7 uniformly distributed MC events using the tessellation of (a), and (c) calculate the CFF values of the 10 million MC events generated in (b), using 40 and 800 cores.

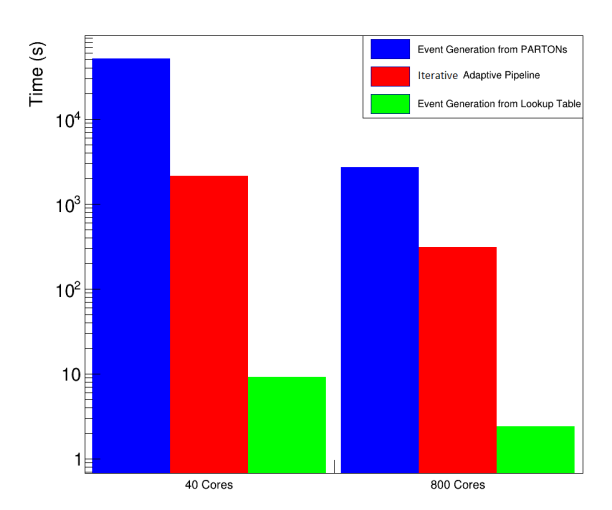


Figure 16: Time comparison to complete the adaptive mesh generation pipeline (red), the time to generate 10 million events by using a mesh as a smart lookup table (green), or directly from PARTONS (blue).

As Figure 16 illustrates, the cost to generate an accurate tessellation of $Im(H_u)$ and 10^7 events using our MC simulation software is 2,151 and 318 seconds using 40 and 800 cores, respectively. The cost to calculate the CFF values of these 10^7 events using just PARTONS is 50,997 and 2694 seconds using 40 and 800 cores, respectively. Consequently, the speedup is 23.7 for 40 cores, and 8.47 for 800 cores. In summary, using 40 cores would take about 35.9 minutes instead of 14.2 hours, and using 800 cores would take about 5.3 minutes instead of 44.9 minutes.

A key take-away is that if someone wanted to generate 10 million MC events again, the cost would be dramatically reduced because the tessellation would have already been generated. Based on the aforementioned performance data, we can derive an estimated generalization of the speed-up formulas for 40 and 800 cores, with respect to the number of events n_e , as shown in Equations 9 and 10.

$$S_c(n_e) = \frac{n_e * T_{PARTONS_c}(1)}{T_{Iterative_adaptive_pipeline_c} + n_e * T_{MC_c}(1)} \approx \frac{n_e * \frac{T_{PARTONS_c}(10^7)}{10^7}}{T_{Iterative_adaptive_pipeline_c} + n_e * \frac{T_{MC_c}(10^7)}{10^7}}$$
(9)

$$S_{40}(n_e) \approx \frac{n_e * \frac{50,997}{10^7}}{2,142 + n_e * \frac{9.2}{10^7}}, \qquad S_{800}(n_e) \approx \frac{n_e * \frac{2,694}{10^7}}{309 + n_e * \frac{2.4}{10^7}}.$$
 (10)

Using these formulas, we estimate that the speedup for generating 10^{10} events would be 4,496 and 994 for 40 and 800 cores, respectively. In summary, one might spend about 3.2 hours instead of 19 months when utilizing 40 cores, or 45.2 minutes instead of 1 month when utilizing 800 cores.

6. Conclusions

In this work, we designed an iterative-adaptive pipeline capable of efficiently generating an adaptive tessellation for a specific Compton Form Factor of a GPD model with a minimal number of vertices while still maintaining a 1% mean interpolation error and a 5% maximum interpolation error. Using such a tessellation as a lookup table significantly decreases the computation time for Monte Carlo event generation, by about 23x for 10^7 events (and using extrapolation, by about 955x for 10^{10} events). Equally as important is the ability to re-use a tessellation multiple times for different analyses without having to do any calculations from a physics model.

In the future, since a GPD model has multiple CFFs, we plan to extend this iterative-adaptive pipeline to generate a *common denominator* adaptive tessellation which satisfies the error threshold for all the CFFs. Generating one tessellation (instead of many) will be beneficial for two reasons: 1) it minimizes the GPD calculations, since PARTONS (the GPD model that we used) calculates all the CFFs at once and 2) MC event generation using multiple tessellations as a lookup table would require the usage of the point location operation (which has $O(log(n^3))$) time complexity) to detect a randomly generated point in another CFF tessellation. The common denominator adaptive tessellation of all the 3-dimensional CFFs, as mentioned in section 4, will be the foundation for efficiently calculating the full DVCS cross section. A potential alternative is to use this iterative-adaptive pipeline to generate a 4-dimensional tessellation of the unpolarized cross section directly from a GPD model. For this purpose, the 4D version of PODM [31] could be enhanced to work with the iterative-adaptive pipeline.

These software tools will be made publicly available to the nuclear physics community in hopes that they are utilized to make a database of tessellation lookup tables of Compton Form Factors and other functions from various physics models.

7. Acknowledgments

This work was funded in part by the Center for Nuclear Femtography (CNF), which is administrated by the Southeastern Universities Research Association (SURA) under an appropriation from the Commonwealth of Virginia, U.S. Department of Energy grant DE-FG02-96ER40960, NSF grant No. CCF-1439079, the Richard T. Cheng Endowment, and the National Institute of General Medical Sciences of the National Institutes of Health under Award Number

1T32GM140911. The content is solely the authors' responsibility and does not necessarily represent the official views of the National Institutes of Health. The performance evaluation was performed using the Wahab computing cluster at Old Dominion University. We would like to thank Min Dong for his assistance in creating the PODM docker image and Emmanuel Billias for reviewing the manuscript and being a Beta-tester for the software.

References

- [1] X. Ji, Gauge-invariant decomposition of nucleon spin, Physical Review Letters 78 (4) (1997) 610.
- [2] F. D. Aaron, et al., Measurement of deeply virtual Compton scattering and its t-dependence at HERA, Phys. Lett. B 659 (2008) 796–806. arXiv:0709.4114, doi:10.1016/j.physletb.2007.11.093.
- [3] S. Chekanov, et al., A Measurement of the Q**2, W and t dependences of deeply virtual Compton scattering at HERA, JHEP 05 (2009) 108. arXiv:0812.2517, doi:10.1088/1126-6708/2009/05/108.
- [4] A. Airapetian, et al., Beam-helicity asymmetry arising from deeply virtual Compton scattering measured with kinematically complete event reconstruction, JHEP 10 (2012) 042. arXiv:1206.5683, doi:10.1007/JHEP10(2012)042.
- [5] R. Akhunzyanov, et al., Transverse extension of partons in the proton probed in the sea-quark range by measuring the DVCS cross section, Phys. Lett. B 793 (2019) 188–194. arXiv:1802.02739, doi:10.1016/j.physletb. 2019.04.038.
- [6] S. Pisano, et al., Single and double spin asymmetries for deeply virtual Compton scattering measured with CLAS and a longitudinally polarized proton target, Phys. Rev. D 91 (5) (2015) 052014. arXiv:1501.07052, doi:10.1103/PhysRevD.91.052014.
- [7] N. Hirlinger Saylor, et al., Measurement of Unpolarized and Polarized Cross Sections for Deeply Virtual Compton Scattering on the Proton at Jefferson Laboratory with CLAS, Phys. Rev. C 98 (4) (2018) 045203. arXiv:1810.02110, doi:10.1103/PhysRevC.98.045203.
- [8] M. Defurne, et al., A glimpse of gluons through deeply virtual Compton scattering on the proton, Nature Commun. 8 (1) (2017) 1408. arXiv:1703.09442, doi:10.1038/s41467-017-01819-3.
- [9] M. Benali, et al., Deeply virtual Compton scattering off the neutron, Nature Phys. 16 (2) (2020) 191–198. arXiv:2109.02076, doi:10.1038/s41567-019-0774-3.
- [10] M. Dlamini, et al., Deep Exclusive Electroproduction of $\pi 0$ at High Q2 in the Quark Valence Regime, Phys. Rev. Lett. 127 (15) (2021) 152301. arXiv:2011.11125, doi:10.1103/PhysRevLett.127.152301.
- [11] A. Accardi, et al., Electron Ion Collider: The Next QCD Frontier: Understanding the glue that binds us all, Eur. Phys. J. A 52 (9) (2016) 268. arXiv:1212.1701, doi:10.1140/epja/i2016-16268-9.
- [12] B. R. Stella, H.-J. Meyer, Υ (9.46 GeV) and the gluon discovery (a critical recollection of PLUTO results), The European Physical Journal H 36 (2) (2011) 203-243. doi:10.1140/epjh/e2011-10029-3. URL https://doi.org/10.48550/arXiv.1008.1869
- [13] J. D. Bjorken, E. A. Paschos, Inelastic electron-proton and γ-proton scattering and the structure of the nucleon, Phys. Rev. 185 (1969) 1975–1982. doi:10.1103/PhysRev.185.1975.
 URL https://link.aps.org/doi/10.1103/PhysRev.185.1975
- [14] A. K. A.V. Belitsky, D. Muller, Theory of deeply virtual compton scattering on the nucleon, Nuclear Physics B 629 (1) (2002) 323–392.
- [15] T. Sjöstrand, S. Ask, J. R. Christiansen, R. Corke, N. Desai, P. Ilten, S. Mrenna, S. Prestel, C. O. Rasmussen, P. Z. Skands, An introduction to PYTHIA 8.2, Comput. Phys. Commun. 191 (2015) 159–177. arXiv:1410.3012, doi:10.1016/j.cpc.2015.01.024.

- [16] C. Bierlich, et al., Pythia 8.3, https://pythia.org/ (Accessed 14 Oct 2021).
- [17] A. A. Johnson, T. E. Tezduyar, Advanced mesh generation and update methods for 3d flow simulations, Computational Mechanics 23 (2) (1999) 130–143.
- [18] F. Drakopoulos, N. P. Chrisochoides, A parallel adaptive physics-based non-rigid registration framework for brain tumor resection, in: International Symposium Computational Modeling of Objects Represented in Images, Springer, 2014, pp. 57–68.
- [19] N. Weatherill, B. Soni, J. Thompson (Eds.), Handbook of Grid Generation, CRC Press, 1998. URL http://www.crcnetbase.com/doi/book/10.1201/9781420050349
- [20] W. M. Chan, J. L. Steger, Enhancements of a three-dimensional hyperbolic grid generation scheme, Applied Mathematics and Computation 51 (2-3) (1992) 181–205.
- [21] S. B. Baden, D. B. Gannon, M. L. Norman, N. P. Chrisochoides, Structured Adaptive Mesh Refinement (Samr) Grid Methods, Springer-Verlag, Berlin, Heidelberg, 1999.
- [22] M. A. Yerry, M. S. Shephard, Automatic three-dimensional mesh generation by the modified-octree technique, International Journal for Numerical Methods in Engineering 20 (11) (1984) 1965–1990.
- [23] G. Kindlmann, J. Bigler, D. Van Uitert, Nrrd file format (2008).
- [24] H. J. Johnson, M. M. McCormick, L. Ibanez, The ITK Software Guide: Design and Functionality (4th ed.), Kitware Inc., 2015. URL https://www.itk.org
- [25] U. Ayachit, The ParaView Guide: A Parallel Visualization Application, Kitware, Inc., Clifton Park, NY, USA, 2015.
- [26] P. A. Foteinos, N. P. Chrisochoides, High quality real-time image-to-mesh conversion for finite element simulations, Journal of Parallel and Distributed Computing 74 (2) (2014) 2123–2140.

 URL https://cepm.cs.odu.edu/pub/papers/journal_56.pdf
- [27] P. J. Roache, Quantification of uncertainty in computational fluid dynamics, Annual review of fluid Mechanics 29 (1) (1997) 123–160.
- [28] K. J. Fidkowski, D. L. Darmofal, Review of output-based error estimation and mesh adaptation in computational fluid dynamics, AIAA journal 49 (4) (2011) 673–694.
- [29] W. Schroeder, K. Martin, B. Lorensen, The Visualization Toolkit (4th ed.), Kitware Inc., 2020. URL https://www.vtk.org
- [30] C. Grimme, Picking a uniformly random point from an arbitrary simplex, Tech. rep., Technical report, Information Systems and Statistics, Munster U., Germany (2015). doi:10.13140/RG.2.1.3807.6968.
- [31] P. Foteinos, N. Chrisochoides, 4d space—time delaunay meshing for medical images, Engineering with Computers 31 (3) (2015) 499–511. doi:10.1007/s00366-014-0380-z. URL https://doi.org/10.1007/s00366-014-0380-z